Ultrasonics - Sonochemistry 54 (2019) 1–10

Contents lists available at ScienceDirect

Ultrasonics - Sonochemistry

journal homepage: www.elsevier.com/locate/ultson

Structural, optical and magnetic properties of Tm^{3+} substituted cobalt spinel ferrites synthesized via sonochemical approach

M.A. Almessiere[a,c,*], Y. Slimani[b,*], A.D. Korkmaz[d], S. Guner[e], M. Sertkol[f], Sagar E. Shirsath[g], A. Baykal[a]

[a] Department of Nanomedicine Research, Institute for Research and Medical Consultations (IRMC), Imam Abdulrahman Bin Faisal University, P.O. Box 1982, 31441 Dammam, Saudi Arabia
[b] Department of Biophysics, Institute for Research and Medical Consultations (IRMC), Imam Abdulrahman Bin Faisal University, P.O. Box 1982, 31441 Dammam, Saudi Arabia
[c] Department of Physics, College of Science, Imam Abdulrahman Bin Faisal University, P.O. Box 1982, 31441 Dammam, Saudi Arabia
[d] Department of Chemistry, Istanbul Medeniyet University, 34700 Istanbul, Uskudar, Turkey
[e] Institute of Inorganic Chemistry, RWTH Aachen University, D-52074 Aachen, Germany
[f] Deanship of Preparatory Year Building 450, Imam Abdulrahman Bin Faisal University, P.O. Box 1982, 31441 Dammam, Saudi Arabia
[g] School of Materials Science and Engineering, University of New South Wales, Kensington, Sydney, NSW 2052, Australia

ARTICLE INFO

Keywords:
Co spinel ferrite
Rare earth element
X-ray diffraction
Microstructure
Magnetic properties
Optical properties

ABSTRACT

Co-Tm nano-spinel ferrite with chemical formula $CoTm_xFe_{2-x}O_4$ ($0.0 \le x \le 0.08$) NPs were prepared via sonochemical approach. X-ray powder diffraction patterns, microscopic images (SEM and TEM) and infrared spectra proved the formation of Co spinel ferrite. The effect of Tm^{3+} substituted on spinal structure was evaluated by lattice parameters, tetrahedral and octahedral bond length and cationic distribution. The band gap energy (Eg) of samples were estimated by performing UV–Vis percent diffuse reflectance (% DR) and applying the Kubelka-Munk theory. Eg values are in an interval between 1.33 eV and 1.64 eV. The analyses of magnetization were performed at room (300 K; RT) and low (10 K) temperatures. Different magnetic parameters including coercivity H_c, saturation magnetization M_s, remanence M_r, squareness ratio (SQR = M_r/M_s) and magnetic moment n_B were deduced and discussed. The results showed superparamagnetic (SPM) nature at RT for x = 0.00 and 0.02 samples. However, the other products exhibit ferromagnetic (FM) nature. At 10 K, all synthesized NPs display FM behavior. An amazing increase in the magnitudes of M_s, M_r and H_c was observed at 10 K in comparison to RT, which is principally due to the reduced thermal fluctuations of magnetic moments at lower temperatures. The Tm^{3+} substitution affects considerably the magnetizations data. An enhancement in the M_s, M_r, and n_B was detected on increasing the Tm^{3+} concentration. The SQR values at RT are found to be smaller than 0.5 postulating a single domain nature with uniaxial anisotropy for all produced ferrites. However, SQRs are in the range 0.66–0.76 at 10 K, suggesting the multi magnetic domain at low temperature, except the x = 0.02 product where the SQR = 0.47 indicating the single magnetic domain. The obtained magnetic results were investigated deeply with relation to structural and microstructural properties.

1. Introduction

All spinel ferrites are scientifically and technologically important. $CoFe_2O_4$ spinel is an attractive material due to its good chemical-thermal stability (even under corrosive conditions), high coercivity, large magneto-crystalline anisotropy, adequate M_s, and high Curie temperature and electrical resistivity [1–5]. They are frequently used in microwave devices, high frequency data storage, memory core and recording media, biotechnology, catalysis, targeted drug delivery systems, sensors, high frequency devices and magnetic fluids [6–11].

Unpaired 4f electrons along with the strong spin-orbit coupling exist in rare earth (RE) elements. So, rare earths ions substitution into spinel ferrite structure can create 3d–4f coupling which may alter their various properties (electrical, spectral, structural, and magnetic) [12,13]. Furthermore, the electromagnetic properties of spinel ferrites are governed by ions nature, their distribution between the octahedral (B) and

* Corresponding authors at: Department of Nanomedicine Research and Department of Biophysics, Institute for Research and Medical Consultations (IRMC), Imam Abdulrahman Bin Faisal University, P.O. Box 1982, 31441 Dammam, Saudi Arabia (M.A. Almessiere and Y.Slimani).
E-mail addresses: malmessiere@iau.edu.sa (M.A. Almessiere), yaslimani@iau.edu.sa (Y. Slimani).

https://doi.org/10.1016/j.ultsonch.2019.02.022
Received 17 January 2019; Received in revised form 13 February 2019; Accepted 24 February 2019
Available online 25 February 2019
1350-4177/ © 2019 Elsevier B.V. All rights reserved.

tetrahedral (A) sites, their oxidation states and ionic sizes [4,14–15].

There are many different routes for preparation of spinel ferrites. Each of them has both advantages and disadvantages. Among these approaches, ultrasonication is different because the chemical effects occur from acoustic cavitation. The implosive collapse of bubbles in solution causes a promptly pressure pulse and high temperature in the solution [16,17]. As a result of this acoustic cavitation, local intense micro-mixing attained [18,19]. The advantages of sonochemical synthesis can be given as: the rate of the ultrasonic chemical reaction is so high due to high number of collisions between reactant molecules. This approach does not need the usage of any other external reagents like surfactant or capping reagents. Besides, it is due to that sonochemical synthesis products have high purity and the reaction environment is “greener”. Furthermode, just by varying the ultrasound frequency and power, the size distribution of products can be easily controlled. Bimetallic alloys and core-shell materials can be synthesized sonochemically at RT, otherwise it would require high reaction temperatures and longer times [20,21].

In this study, we aimed to explore the influence of Tm^{3+} substitution on the structural, microstructural, magnetic and optical properties of $CoFe_2O_4$ NPs produced via ultrasonic irradiation.

2. Experimental

The series of $CoTm_xFe_{2-x}O_4$ ($0.0 \le x \le 0.08$) NPs were synthesized by sonochemical approach. All chemicals obtained from commercial sources (Merck and US Research Nanomaterials, Inc). For the typical synthesis, iron (III) nitrate nonahydrate ($(Fe(NO_3)_3{\cdot}9H_2O)$, cobalt nitrate hexahydrate ($Co(NO_3)_2{\cdot}6H_2O$), Thulium oxide (Tm_2O_3,) were used as a source material for Fe, Co and Tm, respectively. In beaker A, stoichiometric amount of Co and Fe nitrates were dissolved in DI water. The stoichiometric amount of Tm_2O_3 was dissolved in 10 ml conc. HCl (beaker B). Then beaker A and B were mixed together. And then pH of the mixed solution was arranged to 11 via using 2 M NaOH solution. Finally, solution was exposed to high-intensity ultrasonic irradiation (Ultrasonic homogenizer UZ SONOPULS HD 2070; frequency: 20 kHz and power: 70 W) for 60 min. At the end of the ultrasonication, the reaction temperature was measured as 90 °C owing to high number of collisions between the reactants. The received product was washed several times with DI water. The magnetic solid product was separated from the liquid by simple external magnet. It was dried at 60 °C for 12 h.

The composition structure is verified via Rigaku Benchtop Miniflex X-ray powder diffraction (XRD) with CuKα radiation. The morphology was performed by a scanning electron microscope (SEM; FEI Titan ST) coupled with EDX system and transmission electron microscopy (TEM; FEI Morgagni 268). Fourier transform infrared (FT-IR, Bruker) spectra were recorded using a spectrometer over the wavelength range 4000–400 cm^{-1}. The magnetic properties were measured using a Quantum Design SQUID with vibrating sample magnetometer (VSM) head.

3. Results and discussion

3.1. Structural identification

The structure of $CoTm_xFe_{2-x}O_4$ ($0.0 \le x \le 0.08$) NPs were depicted in Fig. 1. All compositions are exhibited the characteristic peaks of major phase of Co spinel ferrite. However, there is a minor phase of Fe_2O_3. The substituted Tm^{3+} ion was dissolved successfully in the spinel structure [20]. It is remarkable that the single phase of Tm substitution cobalt ferrite is prepared only by sonication of metals solution without calcination by pressure using amplitude shock wave produced by the cavitation bubble [21]. The structural parameters are determined by Rietveld refinement for XRD patterns through full proof program. Moreover the tetrahedral and octahedral bond length

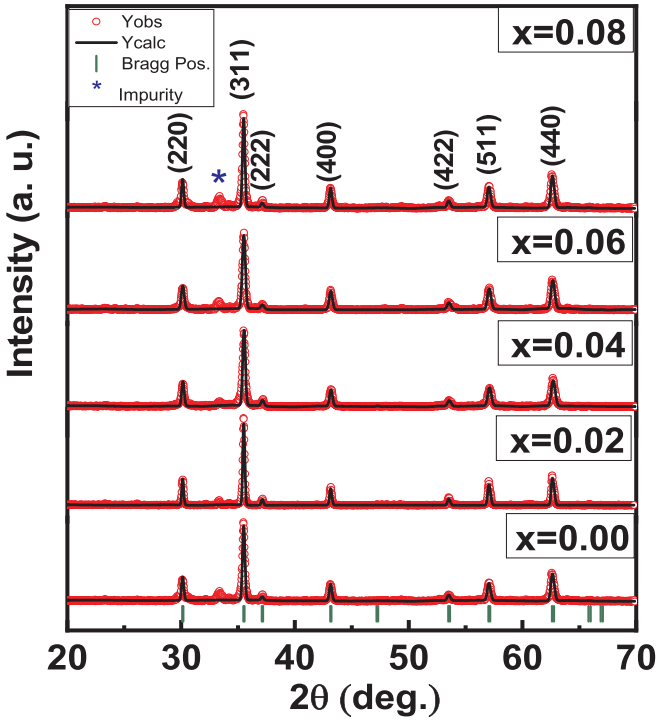

Fig. 1. XRD powder patterns of $CoTm_xFe_{2-x}O_4$ ($0 \le x \le 0.08$) NPs.

Table 1
Tm content, refined structural parameters for $CoTm_xFe_{2-x}O_4$ ($0.00 \le x \le 0.08$) NPs.

Tm content (x)	a (Å)	V (Å^3)	D_{XRD} (nm) ± 0.05	$\chi^2(chi^2)$	R_{Bragg}	d_{AX} (Å)	d_{BX} (Å)
0.00	8.342(1)	580.52	11.08	1.79	3.75	1.87	2.044
0.02	8.380(0)	588.47	44.61	2.86	2.72	1.88	2.053
0.04	8.381(1)	588.71	30.33	1.91	8.60	1.89	2.054
0.06	8.384(5)	589.43	29.26	1.97	3.61	1.89	2.055
0.08	8.388(0)	590.16	35.87	2.51	10.65	1.89	2.056

(d_{AX},d_{BX}) are displayed in Table 1 and determined by the following formulas.

$$d_{AX} = a\sqrt{3}\left(u - \frac{1}{4}\right)$$

$$d_{BX} = a\sqrt{3}\,[3u^2 - (11/4)u + 43/64]^{1/2}$$

where, a is a lattice parameter and u the oxygen positional parameter (0.38 Å) [22]. It is obvious that the significant increasing in d_{BX} compared to d_{AX} with increments of Tm due to the larger radius. The lattice parameter “a” is found to increase with increasing the Tm content due to the expansion into spinel crystal in addition to the lattice microstrain that creates internal stress [23]. Furthermore, the crystallites size is in the range from 11 to 44 nm.

3.1.1. Cation distribution

The site occupancy of cations in $CoTm_xFe_{2-x}O_4$ ($0 \le x \le 0.08$) ferrite system was determined from the well-known Bertaut method based on XRD data. Precisely the following pairs of XRD reflections are express for the Bertaut method.

$$\frac{I_{hkl}^{Obs.}}{I_{h'k'l'}^{Obs.}} \propto \frac{I_{hkl}^{Calc.}}{I_{h'k'l'}^{Calc.}}$$

where, $I_{hkl}^{Obs.}$ stand for observed and $I_{hkl}^{Calc.}$ for calculated intensities for reflection (hkl). respectively. Intensities of (2 2 0), (4 0 0) and (4 4 0) planes were taken into consideration while determining the cation

Table 2
Cation distribution calculations of $CoTm_xFe_{2-x}O_4$ ($0 \le x \le 0.08$) NPs.

x	Tetrahedral A-site	Octahedral B-site
0.0	$Fe_{0.8}Co_{0.2}$	$Fe_{1.2}Co_{0.8}$
0.02	$Fe_{0.8}Co_{0.2}$	$Fe_{1.18}Co_{0.8}Tm_{0.02}$
0.04	$Fe_{0.8}Co_{0.2}$	$Fe_{1.16}Co_{0.8}Tm_{0.04}$
0.06	$Fe_{0.8}Co_{0.2}$	$Fe_{1.14}Co_{0.8}Tm_{0.06}$
0.08	$Fe_{0.8}Co_{0.2}$	$Fe_{1.12}Co_{0.8}Tm_{0.08}$

distribution, since these planes are sensitive to the cation distribution. The cation distribution calculations are independent of temperature and absorption factors [24,25]. Spinel ferrites oxides consist of two crystallographic sites of sublattices namely tetrahedral (A) and the octahedral (B). The cation distribution of $CoTm_xFe_{2-x}O_4$ system is presented in Table 2 The cation distribution for each value of x, indicated that the Fe^{3+} and Co^{2+} ions occupy both tetrahedral A-site and octahedral B-site, whereas Tm^{3+} cation occupy octahedral B-site only.

3.2. Microstructural analysis

The morphologies of $CoTm_xFe_{2-x}O_4$ (x = 0.00, 0.02 and 0.06) NPs are performed and presented in Fig. 2. The images displayed an agglomeration of spherical particles with homogeneous distribution caused by the magnetic interaction amongst these particles. The grains size is around 20 nm and increases with rising the amount of substitution. For proving the effectiveness of preparation method of our samples, the EDX and elemental mapping are employed for $CoTm_xFe_{2-x}O_4$ (x = 0.00, 0.02 and 0.06) NPs as listed in Fig. 3. The samples contain the Co, Tm, Fe and O elements with the correct stoichiometry. In order to verify the particles size and the morphology of $CoTm_xFe_{2-x}O_4$ (x = 0.00, 0.02 and 0.06) NPs, HRTEM and SEAD are carried out as depicted in Fig. 4. The HRTEM analysis indicated the spherical shape. It is revealed that the particles size is less than 50 nm. The SAED patterns offered a continuous ring that confirmed the atomic planes of X-ray patterns. Moreover, these continuous rings are defined well crystalline of the products.

3.3. Infrared spectra

FT-IR spectra of $CoTm_xFe_{2-x}O_4$ ($0.00 \le x \le 0.08$) NPs are presented in Fig. 5. The two characteristic vibration bands of spinel ferrites are presented at 571.76 and 405.4 cm^{-1} related to the vibrations band $\nu 1$, $\nu 2$ of A and B sites, respectively [26]. All samples exhibited identical FT-IR absorption bands performance, which approve the spinel ferrite formation. Moreover, there is no existence of unreacted chemical in the samples. It is obvious that the vibration band at 571.76 cm^{-1} is shifted toward the lower at x = 0.02 then to higher frequencies at the rest of ratios while the 405.4 cm^{-1} mostly remind in the same position for the substitution samples. This variation as a consequence of the deference in length of Fe-O bands at both tetrahedral (A-site) and octahedral (B-site) due to the Tm substituting, as a result of an inverse spinal nature of cobalt ferrite [27,28]. Force constant of FT-IR using characteristic vibration bands have been evaluated for A and B sites by using $F_C = 4\pi^2C^2\nu^2m$, whereas C is velocity of light, m reduced mass of Fe^{3+} and O^{2-} ions which is 2.061×10^{-23} g and $\nu$is vibration bond as listed in Table 3 [29]. It was found that the force constant of tetrahedral (A-site) F_{CT} is fluctuating while the octahedral (B-site) $F_{CO}$is almost stable due to the transfer of Fe^{3+} ion from B-site to A-site [30].

3.4. % DR measurements

Percent Diffuse Reflectance (% DR) investigations were conducted in the range of 200–800 nm to determine optic properties of Tm substituted Co spinel ferrite samples (Fig. 6). The remarkable increases in reflectance from 15% until 42% is observed at the spectrum belongs to $CoTm_{0.02}Fe_{1.98}O_4$ NPs above the wavelength of 600 nm. Other samples have reflectance between 10% and 25% in the near UV and visible region of light. The Kubelka-Munk theory is most widely used to analyze the % DR spectra. The function $F(R_\infty)$ that was derived by Kubelka and Munk, has direct proportionality with the absorption coefficient (α):

$$F(R_\infty) = \frac{(1-R_\infty)^2}{2R_\infty} = \frac{2.303\varepsilon C}{S} = \alpha$$

where R_∞ is the absolute remittance, ε is the absorptivity, C is the analyte concentration and S is the twice the scattering coefficient of the

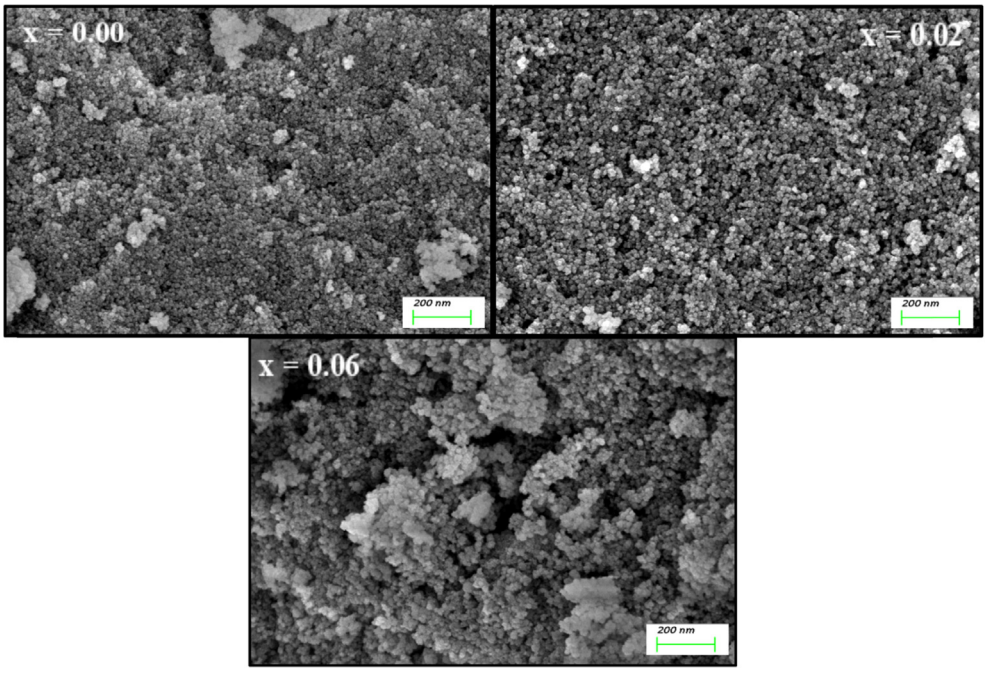

Fig. 2. FE-SEM images of $CoTm_xFe_{2-x}O_4$ (x = 0.00, 0.02 and 0.06) NPs.

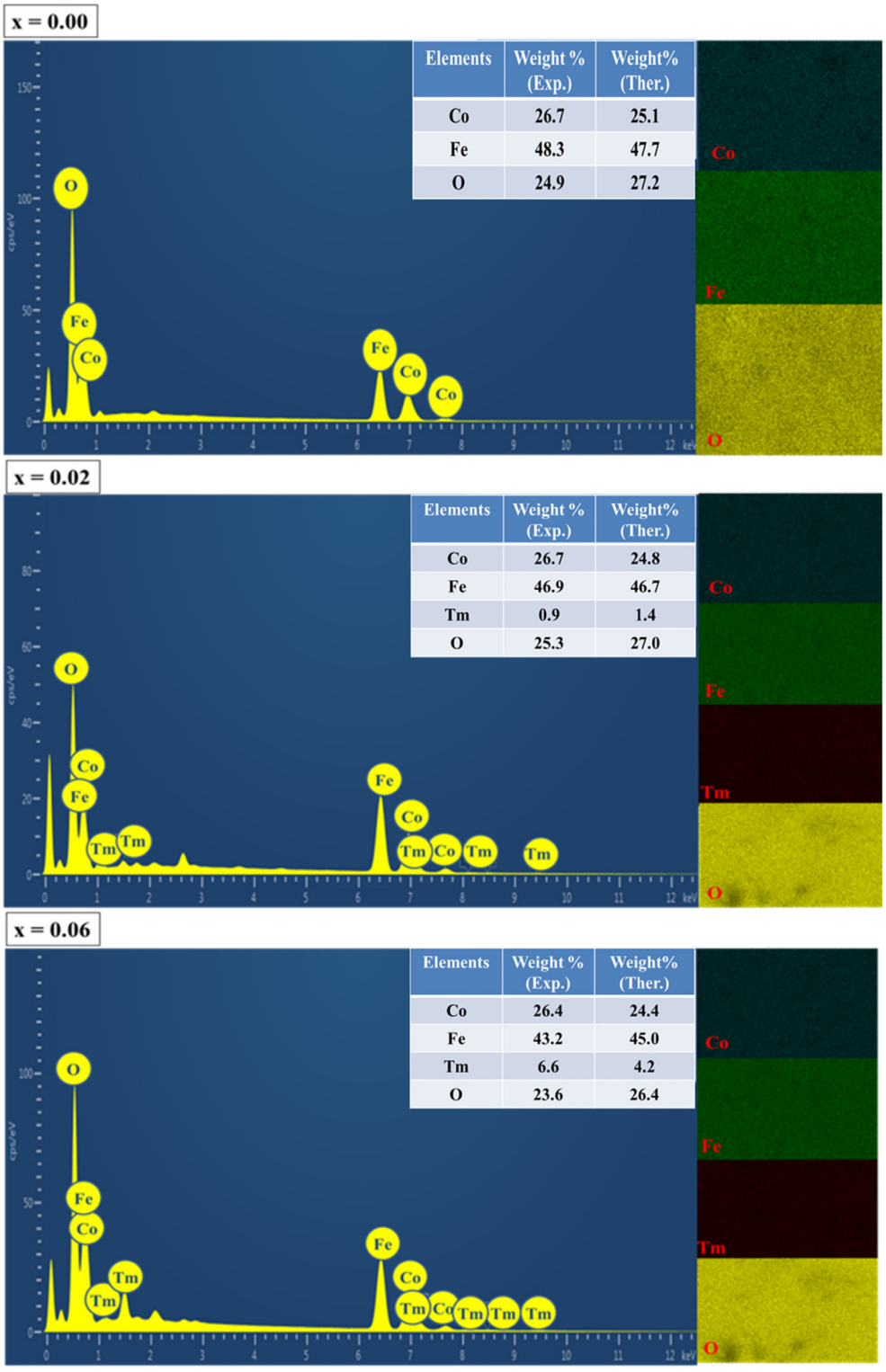

Fig. 3. EDX spectra and elemental mapping of $CoTm_xFe_{2-x}O_4$ (x = 0.00, 0.02 and 0.06) NPs.

sample. Band gap energy (E_g) of the nanoparticulate samples could be determined utilizing Kubelka-Munk function. The correlation between α and the E_g is known as Tauc relation [31–33]. Further, David and Mott indicated that the strength of optical absorption depends on the difference among photon energy (hυ) and E_g as follow [34,35]:

$$(\alpha h\upsilon)^{1/n} = A(h\upsilon - E_g)$$

where h is Planck constant, υ is the photon's energy frequency, A is a proportionality constant and n denotes the nature of electronic transitions:

n = 3/2, transition is direct and forbidden
n = 1/2, transition is direct and allowed
n = 3, transition is indirect and forbidden
n = 2, transition is indirect and allowed.

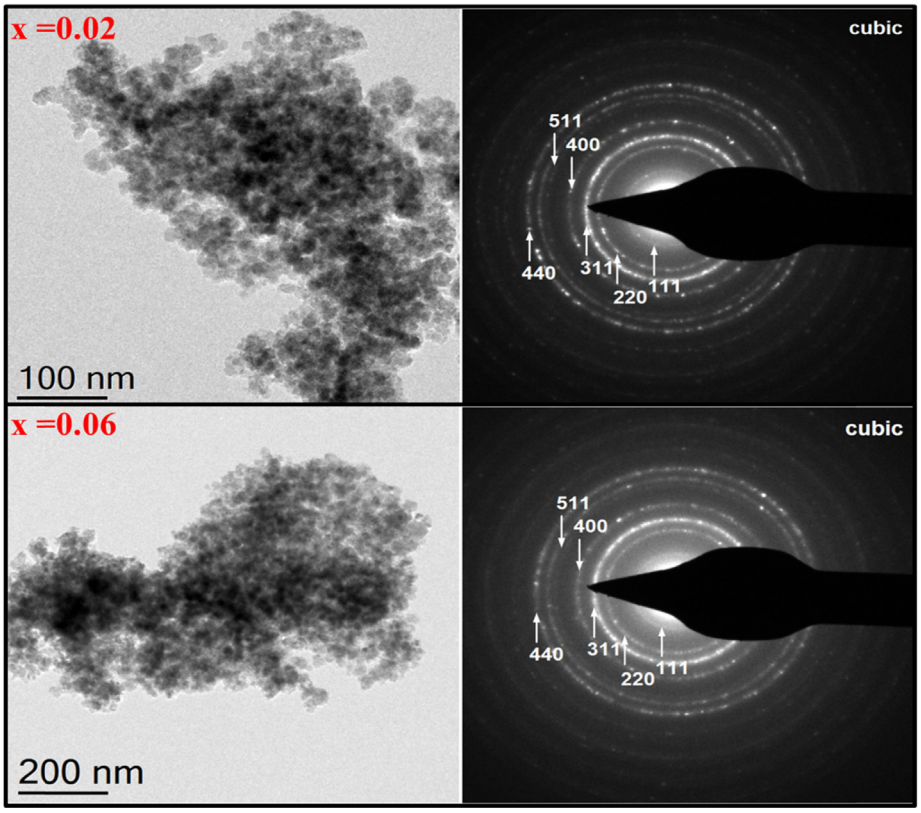

Fig. 4. HR-TEM and SEAD images of $CoTm_xFe_{2-x}O_4$ (x = 0.02 and 0.06) NPs.

Fig. 7 presents Tauc plots of $CoTm_xFe_{2-x}O_4$ ($0 \le x \le 0.08$) NPs with n = 1/2. In the Tauc plots, the absorption is strong and exhibits a linearity near E_g. Therefore, it is used to extrapolate to the x-axis intercept to determine E_g values. The extrapolated E_g for pristine $CoFe_2O_4$ NPs is 1.33 eV and substituted $CoTm_{0.02}Fe_{1.98}O_4$ NPs has 1.64 eV. As seen from Table 1, crystallite sizes of 11 nm and 44 nm are also belonging to these two samples, respectively. All the others have close crystallite sizes around 32 nm and band gap values around 1.50 eV. Tm^{3+} ion substitution caused significant increase at crystallite sizes of NPs. The important role of crystallite size on the band gap values is also reported in the literature [36,37]. Pristine $CoFe_2O_4$ NPs with 11 nm crystallite sizes are in the quantum confinement regime. In other words, the quantum size effect (QSE) plays the major role for E_g value. Tm^{3+} ion substituted NPs with 29.26 nm or larger crystallite sizes are beyond this regime. However, the effect of decrease at crystallite size from 44 nm to average 32 nm seems to be main reason to observe decrease from 1.64 eV to average 1.50 eV optical band gap values. In the literature, there are reported optical band gap data mainly for pristine or substituted $CoFe_2O_4$ NPs with different elements except Tm^{3+} ion [38–41]. They report E_g values in a wide interval of 1.90–3.85 eV. However, the results reported by Quinonez et al. are in great accordance with our data [42].

3.5. Magnetization investigations

The plots of magnetization against an applied magnetic field up to ± 70 kOe, M(H), for different $\mathbf{CoTm_xFe_{2-x}O_4}$ ($0.00 \le x \le 0.08$) NPs performed at RT are illustrated in Fig. 8a. Fig. 8b shows magnetic hysteresis loops in the range ± 6 kOe. The various deduced magnetic parameters for all prepared NPs at RT are summarized in Table 4. The detailed analyses revealed that the Tm^{3+} substitution in Fe^{3+} sites cause remarkable changes at magnetization characteristics of hysteresis loops. The M_{max} values (magnetization at maximum field of 70 kOe) are ranging from 48.96 to 78.63 emu/g at RT. The Stoner–Wohlfarth (S–W) theory is used to extract the saturation magnetization (M_s) [43–45]. Fig. 9 shows the plots of M versus $1/H^2$ for all $\mathbf{CoTm_xFe_{2-x}O_4}$ ($0.00 \le x \le 0.08$) NPs performed at RT. The extrapolation of these plots, at high fields, in approaching 0 offers the M_s values. The different Tm substituted Co ferrite NPs exhibit M_s values varying between 49.56 and 79.64 emu/g at RT. The non-substituted $CoFe_2O_4$ sample (x = 0.00) display M_r and H_c values at RT equal to 0.81 emu/g and 15.06 Oe, respectively. The substituted Co ferrite with Tm content of 0.02 exhibit M_r and H_c values at RT equal to 1.97 emu/g and 20.23 Oe, respectively. The obtained M_r and H_c values at RT for x = 0.00 and 0.02 samples are very small, which indicates that these two products exhibit superparamagnetic (SPM) nature at RT. Except the x = 0.00 and 0.02 ones, the other synthesized $\mathbf{CoTm_xFe_{2-x}O_4}$ NPs with Tm content ranging between 0.04 and 0.08 revealed higher M_r and H_c values at RT. These $\mathbf{CoTm_xFe_{2-x}O_4}$ ($0.04 \le x \le 0.08$) NPs display M_r ranging from 21.45 to 23.61 emu/g. The H_c is in the 840.61–894.94 Oe range. Accordingly, one can affirm that the Tm substituted Co ferrite NPs with $0.04 \le x \le 0.08$ present soft ferromagnetic (FM) nature at RT.

The M(H) were also performed for all $\mathbf{CoTm_xFe_{2-x}O_4}$ ($0.00 \le x \le 0.08$) NPs at 10 K and H = ± 70 kOe (Fig. 10a). The registered hysteresis curves are given in Fig. 10b between −30 kOe and +30 kOe. The deduced magnetic parameters at 10 K are listed in Table 5. H_c varies between 1168.99 and 10908.5 Oe. M_r is in the range 48.79–68.79 emu/g. The M_{max} values are in 62.88–145.03 emu/g range. M_s are determined also using S-W approximation and found to vary between 63.85 and 146.32 emu/g. The obtained magnetic results at 10 K are non-negligible, which reveal the hard FM nature of all Tm^{3+} substituted Co ferrite NPs at 10 K. The M_s, M_r and H_c magnitudes show an amazing increase at 10 K compared to those at 300 K. The increment is principally due to the reduced thermal fluctuations of magnetic moments [46,47]. Furthermore, the anisotropy contribution of rare-earth ions is reported in previous studies to be via spin-orbit coupling when they occupy B sites [44,48]. This is one of the causes to observe higher coercivities at Co ferrites doped with rare-earth ions.

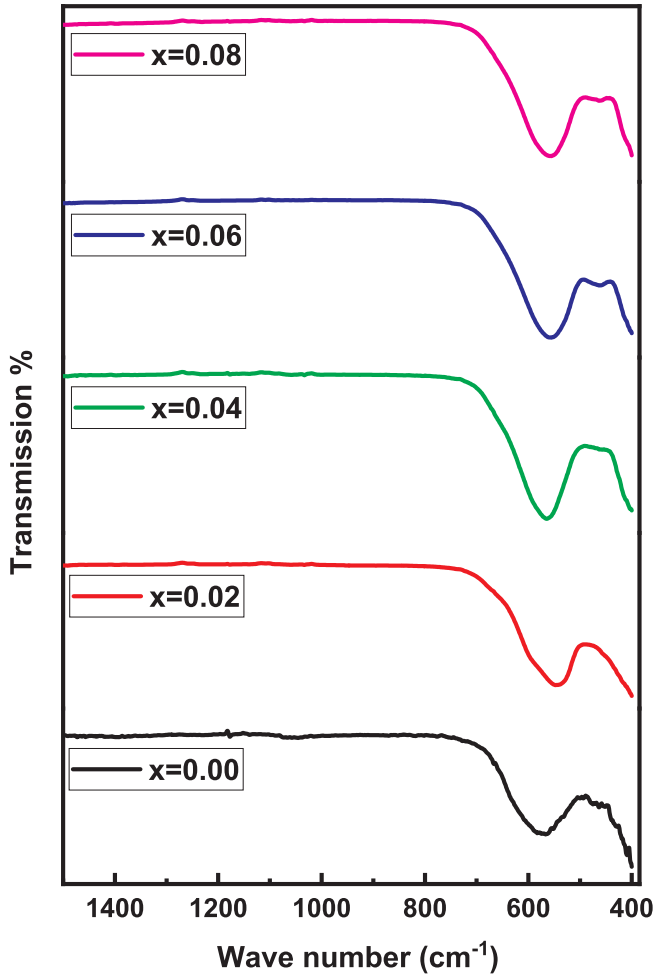

Fig. 5. FT-IR spectra of $CoTm_xFe_{2-x}O_4$ ($0 \le x \le 0.08$) NPs.

Table 3
FTIR vibration bands and force constant at tetrahedral and octahedral positions of $CoTm_xFe_{2-x}O_4$ ($0.00 \le x \le 0.08$) NPs.

Tm content (x)	(ν1) cm^{-1}	(ν2) cm^{-1}	$F_{CT} \times 10^5$ (dynes/cm^2)	$F_{CO} \times 10^5$ (dynes/cm^2)
0.00	571.76	405.40	2.456	1.231
0.02	543.48	401.38	2.219	1.210
0.04	563.68	401.47	2.387	1.211
0.06	559.60	401.47	2.353	1.211
0.08	559.64	401.42	2.353	1.211

At RT, the H_c values are lower than 25 Oe for $x \le 0.02$ and are in the range of 840.61–894.94 Oe for $0.04 \le x \le 0.08$. At 10 K, the coercivity is minimum for x = 0.02 samples with value of 1168.99 Oe. The maximum H_c magnitude at 10 K is observed for the x = 0.00 sample with value equal to 10908.5 Oe. Largely, various parameters influenced the coercivity like morphology, grains size, shape and magneto-crystalline anisotropy, etc [49,50]. At both measurement temperatures, the x = 0.00 one has the lowest magnitudes of M_s, which are about 49.56 and 63.85 emu/g at 300 and 10 K, respectively. It is found that the Tm^{3+} substitution content lead to increase in a remarkable way the M_s. The M_s values are in the range of 66.19–79.64 emu/g at RT and 83.81–146.32 at 10 K for all substituted $\mathbf{CoTm_xFe_{2-x}O_4}$ ($0.02 \le x \le 0.08$) NPs. The highest M_s magnitudes with values of about 79.64 and 146.32 emu/g at 300 and 10 K, respectively are noted for the x = 0.02 one. The magnetization magnitudes found in the present study for x = 0.02 sample greater than those

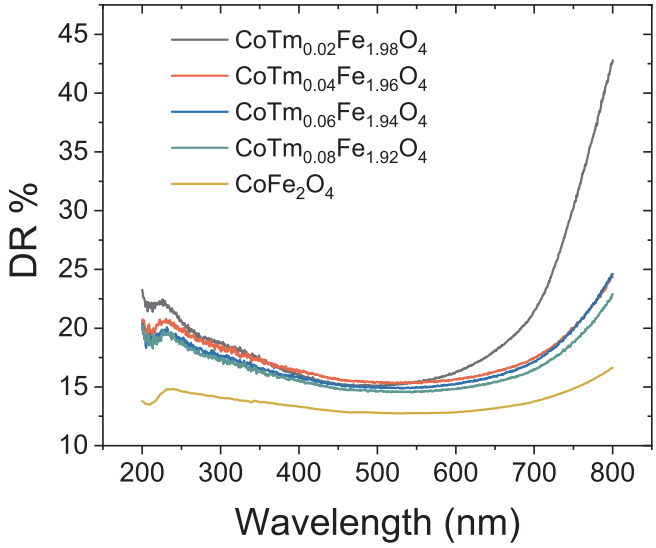

Fig. 6. %DR spectra of $CoTm_xFe_{2-x}O_4$ ($0 \le x \le 0.08$) NPs in the near UV and visible region.

reported in many other substituted Co ferrites such as rare-earth (RE = Nd, Sm and Gd) substituted Co ferrite NPs, Cr substituted Co nano-ferrites, Al substituted Co-ferrite NPs, In doped Co ferrites, etc [51–54]. Moreover, it was observed that the evolutions in the M_r values show practically the similar trend of M_s with respect to the Tm^{3+} concentration. It is reported previously that evolutions in M_r depends predominantly on evolutions in M_s and also on the net alignment of magnetization grains derived from super exchange interactions between MNPs [49,55–61]. It is well known that numerous factors can affect the magnetization of spinel ferrites including the crystallites size change, variations in magnetic moments (n_B), variations in the nature and concentration of different sites, and favorite site occupancy of different ions, etc [48–50,62]. As well, the local strains and the super exchange interactions between different ions might have an influence on magnetic parameters [46,48]. Principally, the magnetic moment in spinel ferrites is derived from iron ions and their distribution in the crystal sites. Moreover, the B-B and A-A interactions are unimportant, however, the A-B exchange interactions are the dominant. Consequently, any factors affecting the strength of various exchange interactions will modify the magnetization. In our case, the observed increase in magnetization values with Tm^{3+} substitution is attributable to the exchange interactions strengthening in Fe sites. We remind that the ions of host Fe^{3+} (0.62 Å) display smaller ionic radius compared to that of Tm^{3+} (0.87 Å). This contrast might engender non-collinear ferromagnetic arrangement and local strains that lead to a disorder and variations of electronic states [46,50,63,64].

In addition, the contrast of ionic radii results in reducing the distance separating the magnetic ions and therefore increasing the strength of A-B super exchange interactions. The relation between magnetic moment (n_B) and M_s is given by [65]:

$$n_B = \frac{Molecular\ Weight \times M_s}{5585}$$

The estimated n_B values of all $\mathbf{CoTm_xFe_{2-x}O_4}$ ($0.00 \le x \le 0.08$) NPs at 300 and 10 K are summarized in Tables 4 and 5, respectively. It is well-known that the increase in n_B values is resulting from the strengthening of the superexchange interactions among various sites. In this study, compared to x = 0.00, n_B is found to rise for x = 0.02 and then decrease with further increasing Tm^{3+} concentration. One should note that the values of n_B for various substituted samples at RT and 10 K are higher than those of non-substituted one. It is noticed that the x = 0.02 sample in which M_s value is the highest, displays the greatest n_B. Also, the x = 0.00 sample in which M_s value is the lowest, displays

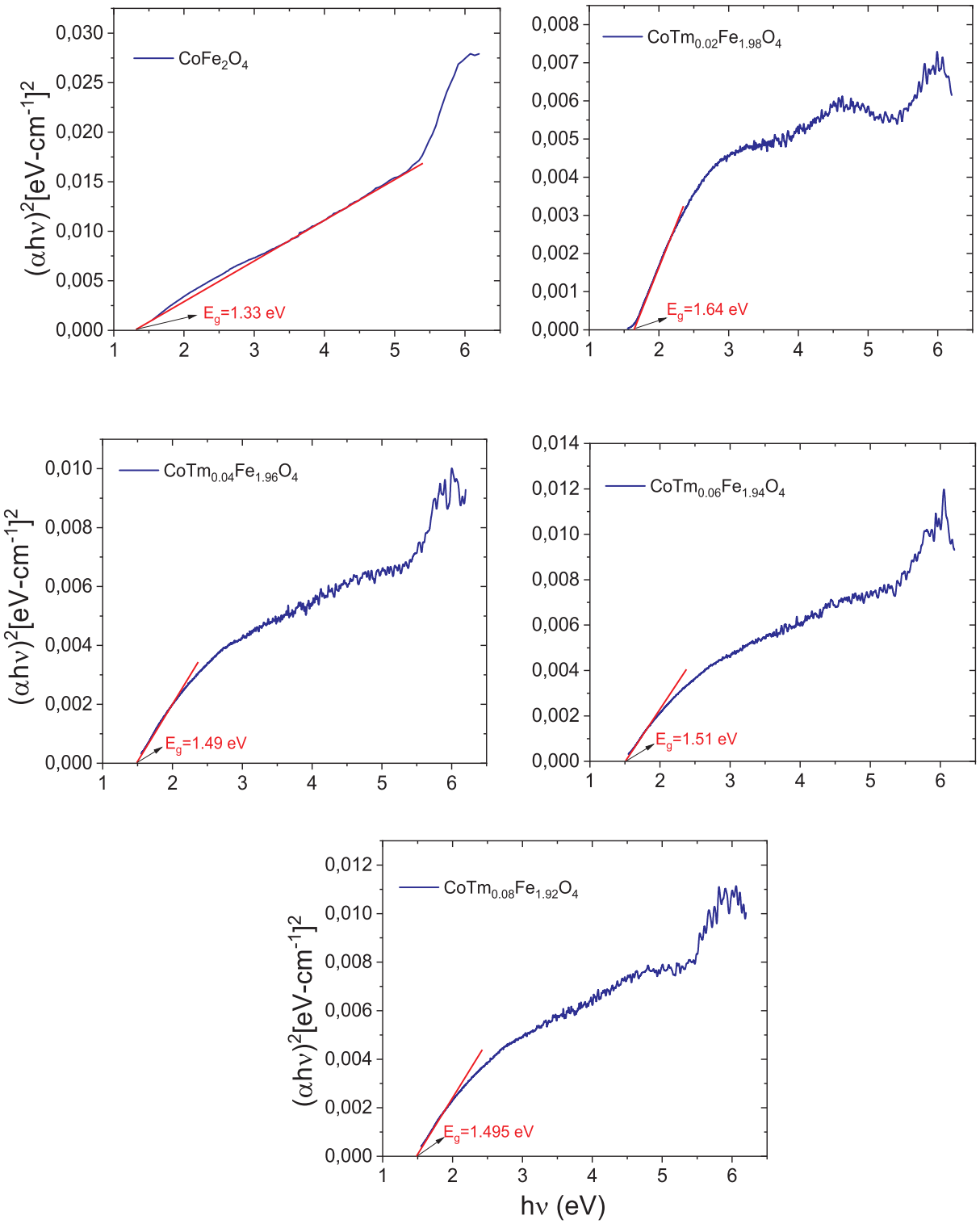

Fig. 7. Tauc plots of $CoTm_xFe_{2-x}O_4$ ($0 \le x \le 0.08$) NPs. The fitting of linear region at the x-axis intercept determines the value of optical band gap.

the lowest n_B. This indicates that the super-exchange interaction is strengthened with Tm substitution.

The squareness ratios ($SQR = M_r/M_s$) were calculated for all **$CoTm_xFe_{2-x}O_4$** ($0.00 \le x \le 0.08$) NPs at 300 and 10 K (Tables 4 and 5). According to S-W theory, the SQR can take two values: one around 0.83 associated to cubic anisotropy and another around 0.5 correspond to uniaxial anisotropy [43,44]. Furthermore, it is reported that the $SQR \ge 0.5$ suggests that nanoparticles are in a single magnetic domain and $SQR < 0.5$ mostly ascribed to the development of multi-domain structure [66]. As can be seen from the tables, the SQRs for all **$CoTm_xFe_{2-x}O_4$** ($0.00 \le x \le 0.08$) NPs at RT were found in the range of 0.016–0.324 suggesting the single magnetic domain with uniaxial anisotropy. Furthermore, the SQR values at RT are less than 0.50, which could be accredited also to the effects of surface spin disorder. At 10 K, except the x = 0.02 sample which display SQR of about 0.470 suggesting the single magnetic domain with uniaxial anisotropy in this sample, the other products exhibit SQRs in the range of 0.662–0.764 indicating the formation of multi magnetic domain.

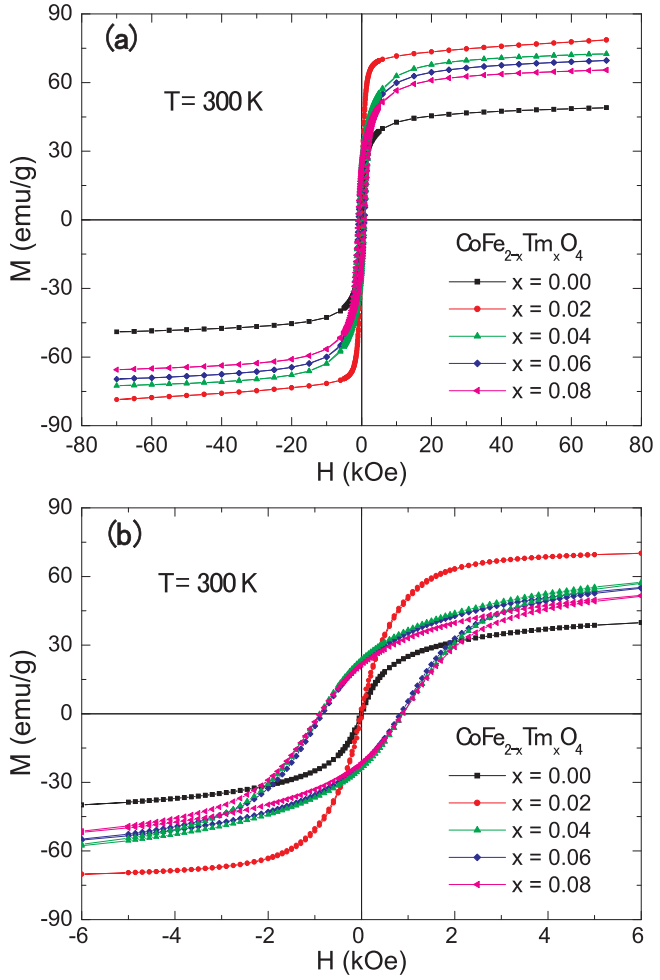

Fig. 8. (a) M(H) hysteresis loops under an applied field up to ± 70 kOe of $CoFe_{2-x}Tm_xO_4$ ($0.00 \le x \le 0.08$) NPs at RT. (b) An enlarged view of M(H) curves in H = ± 6 kOe.

Table 4
The deduced magnetic parameters of all $Co_5Fe_{2-x}Tm_xO_4$ ($0.00 \le x \le 0.08$) NPs at RT.

x	M_{max} (emu/g)	M_s (emu/g)	M_r (emu/g)	SQR	H_c (Oe)	$n_B(\mu_B)$
0.00	48.96	49.56	0.81	0.016	15.06	2.08
0.02	78.63	79.64	1.97	0.025	20.23	3.38
0.04	72.53	73.25	23.61	0.322	894.94	3.14
0.06	69.67	70.51	22.06	0.313	840.61	3.05
0.08	65.47	66.19	21.45	0.324	886.54	2.89

4. Conclusion

Tm substituted Cobalt spinel ferrite NPs are synthesized by sono-chemical method. The XRD approved the creation of the cubic structure of spinel ferrite. The crystallites size is in the range of 11 to 44 nm. Cationic distribution is employed to confirm the occupation B-site by Tm ions. FE-SEM and HR-TEM showed the spherical morphology with high rate of agglomeration. % DR investigations assign the direct E_g values between 1.33 and 1.64 eV. Crystallite size play more significant role with respect to ion content at E_g values. These magnitudes lie in the semiconductor band gap range. Tm ion substitution, especially x = 0.02 ratio, cause significant changes at Eg values. The M(H) analyses performed at RT show an almost SPM comportment for x = 0.00 and 0.02 samples and a FM behavior for $x \ge 0.04$. At 10 K, a FM behavior is observed in various Tm^{3+} substituted Co ferrite NPs. The magnetic

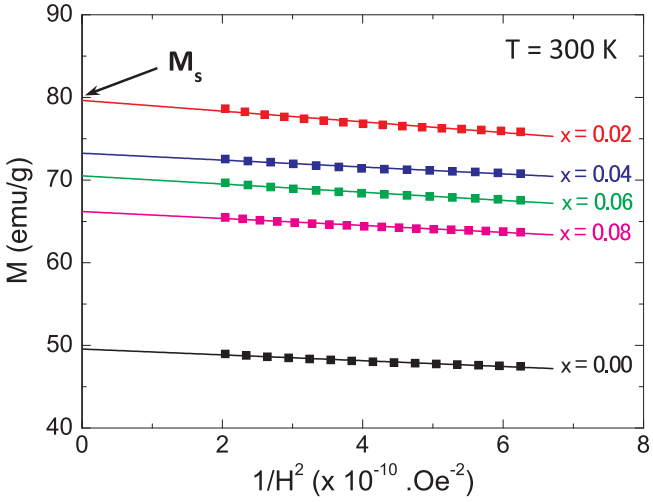

Fig. 9. Plots of M vs $1/H^2$ $CoFe_{2-x}Tm_xO_4$ ($0.00 \le x \le 0.08$) NPs at RT.

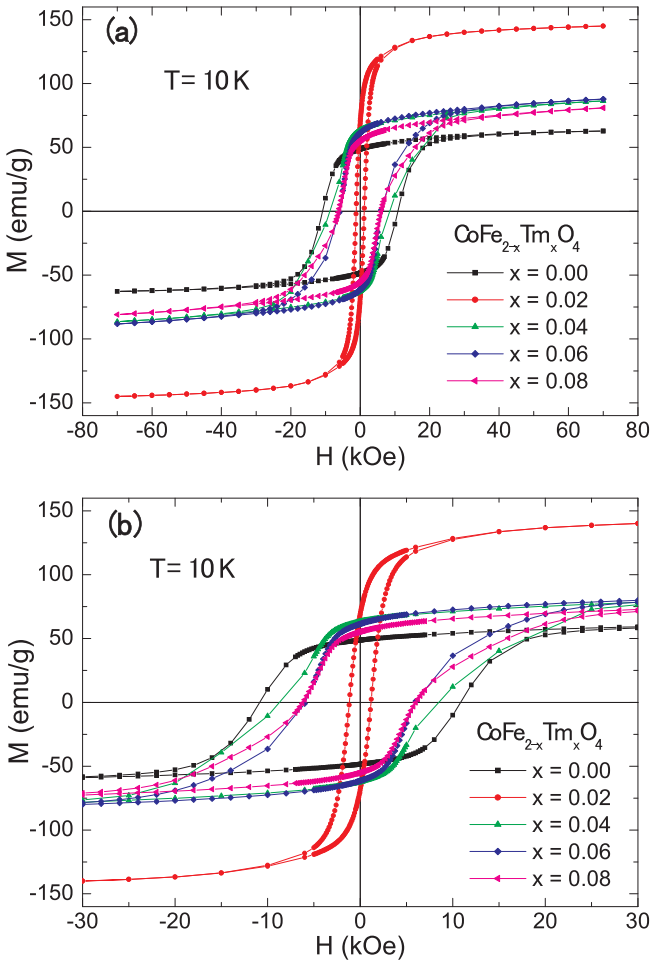

Fig. 10. (a) M(H) hysteresis loops under an applied field up to ± 70 kOe of $CoFe_{2-x}Tm_xO_4$ ($0.00 \le x \le 0.08$) NPs performed at 10 K. (b) An enlarged view of M(H) curves in H = ± 30 kOe.

parameters strongly depend on temperature and on Tm substitution contents. An amazing increase in the magnitudes of M_s, M_r and H_c was observed at 10 K in comparison to RT. The Tm^{3+} substitution leads to enhance the magnetization. The deduced M_s values at both temperatures are maximum for x = 0.02 sample. This effect is due to the strengthening of super-exchange interactions, the creation of local

Table 5
The deduced magnetic parameters of all $Co_5Fe_{2-x}Tm_xO_4$ ($0.00 \leq x \leq 0.08$) NPs at 10 K.

x	M_{max} (emu/g)	M_s (emu/g)	M_r (emu/g)	SQR	H_c (Oe)	$n_B(\mu_B)$
0.00	62.88	63.85	48.79	0.764	10908.5	2.68
0.02	145.03	146.32	68.79	0.470	1168.99	6.21
0.04	87.81	90.01	63.41	0.704	8783.64	3.85
0.06	86.43	88.68	61.48	0.693	5983.85	3.83
0.08	81.02	83.81	55.51	0.662	6206.67	3.66

strains, the preferred site occupancy and the increase in the magnetic moments (n_B) with respect to Tm^{3+} content. The SQR values at RT are found to be smaller than 0.5, which postulate the single domain nature with uniaxial anisotropy for all produced ferrites. At 10 K, the x = 0.02 product display SQR values equal to 0.47, which indicate the single magnetic domain. The other products display SQRs in the range 0.66–0.76 at 10 K suggesting the multi-magnetic domain in these samples.

Acknowledgements

The Institute for Research and Medical Consultations (IRMC) of Imam Abdulrahman Bin Faisal University (IAU – Saudi Arabia) is highly acknowledged for providing the supports through the Projects application No. 2018-IRMC-S-1, No. 2018-IRMC-S-2 and No. 2017-IRMC-S-3.

References

[1] Y.K. Elayakumar, A. Dinesh, A. Manikandan, Murugesan Palanivelu, G. Kavitha, S. Prakash, R. Thilak Kumar, Saravana Kumar Jaganathani, A. Baykal, Structural morphological, enhanced magnetic properties and antibacterial bio-medical activity of rare earth element (REE) cerium (Ce^{3+}) doped $CoFe_2O_4$ nanoparticles, J. Magn. Magn. Mater. 476 (2019) 157–165.

[2] A. Manikandan, R. Sridhar, S. Arul Antony, Seeram Ramakrishna, A simple aloe vera plant-extracted microwave and conventional combustion synthesis: morphological, optical, magnetic and catalytic properties of $CoFe_2O_4$ nanostructures, J. Mol. Struct. 1076 (2014) 188–200.

[3] M.A. Almessiere, Y. Slimani, S. Güner, M. Nawaz, A. Baykal, F. Aldakheel, S. Akhtar, I. Ercan, İ. Belenli, B. Özçelik, Magnetic and structural characterization of Nb^{3+}-substituted $CoFe_2O_4$ nanoparticles, Ceram. Int. (2019), https://doi.org/10.1016/j.ceramint.2019.01.125.

[4] A. Manikandan, M. Durka, S. Arul Antony, A novel synthesis, structural, morphological, and opto-magnetic characterizations of magnetically separable spinel $Co_xMn_{1-x}Fe_2O_4$ ($0 \leq x \leq 1$) nano-catalysts, J. Supercond. Novel Magn. 27 (2014) 2841–2857.

[5] E. Hema, A. Manikandan, P. Karthika, S. Arul Antony, B.R. Venkatraman, A novel synthesis of Zn^{2+}-doped $CoFe_2O_4$ spinel nanoparticles: structural, morphological, opto-magnetic and catalytic properties, J. Supercond. Novel Magn. 28 (2015) 2539–2552.

[6] A. Godlyn Abraham, A. Manikandan, E. Manikandan, S. Vadivel, S.K. Jaganathan, A. Baykal, Enhanced magneto-optical and photo-catalytic properties of transition metal cobalt (Co^{2+} ions) doped spinel $MgFe_2O_4$ ferrite nanocomposites, J. Magn. Magn. Mater. 452 (2018) 380–388.

[7] A. Hannour, D. Vincent, F. Kahlouche, A. Tchangoulian, S. Neveu, V. Dupuis, Self-biased cobalt ferrite nanocomposites for microwave applications, J. Magn. Magn. Mater. 353 (2014) 29.

[8] K.A. Manikandan, E. Manikandan, B. Meenatchi, S. Vadivel, S.K. Jaganathan, R. Ladchumananandasivam, M. Henini, M. Maaza, Jagathrakshakan Sundeep Aanand, Rare earth element (REE) lanthanum doped zinc oxide (La: ZnO) nanomaterials: synthesis structural optical and antibacterial studies, J. Alloys Compd. 723 (2017) 1155–1161.

[9] R. Bomila, S. Srinivasan, S. Gunasekaran, A. Manikandan, Enhanced photocatalytic degradation of methylene blue dye, opto-magnetic and antibacterial behaviour of pure and La-doped ZnO nanoparticles, J. Supercond. Nov. Magn. 31 (2018) 855–864.

[10] H. Tombuloglu, G. Tombuloglu, Y. Slimani, I. Ercan, H. Sozeri, A. Baykal, Impact of manganese ferrite (MnFe2O4) nanoparticles on growth and magnetic character of barley (*Hordeum vulgare* L.), Environ. Pollut. 243 (2018) 872–881.

[11] K. Elayakumar, A. Manikandan, A. Dinesh, K. Thanrasu, K. Kanmani Raja, R. Thilak Kumar, Y. Slimani, S.K. Jaganathangh, A. Baykal, Enhanced magnetic property and antibacterial biomedical activity of Ce^{3+} doped $CuFe_2O_4$ spinel nanoparticles synthesized by sol-gel method, J. Magn. Magn. Mater. (2019), https://doi.org/10.1016/j.jmmm.2019.01.108.

[12] S. Mahalakshmi, K. Srinivasa, K. Manja, S. Nithiyanantham, Electrical properties of nanophase ferrites doped with rare earth ions, J. Superconduct. Novel Magn. 27 (2014) 2083–2088.

[13] A. Zubair, Z. Ahmad, A. Mahmood, W.C. Cheong, I. Ali, M.A. Khan, A.H. Chughtai, M.N. Ashiq, Structural, morphological and magnetic properties of Eu-doped $CoFe_2O_4$ nano-ferrites, Results Phys. 7 (2017) 3203–3208.

[14] C. Murugesan, G. Chandrasekara, Impact of Gd^{3+} substitution on the structural, magnetic and electrical properties of cobalt ferrite nanoparticles, RSC Adv. 5 (2015) 73714–73725.

[15] A. Manikandan, M. Durka, S. Arul Antony, Role of Mn^{2+} doping on structural, morphological, and opto-magnetic properties of spinel $MnxCo_{1-x}Fe_2O_4$ (x = 0.0, 0.1, 0.2, 0.3, 0.4, and 0.5) nanocatalysts, J. Supercond. Nov. Magn. 28 (2015) 2047–2058.

[16] Raghvendra Singh Yadava, Ivo Kuřitkaa, Jarmila Vilcakova, Jaromir Havlicab, Lukas Kalinab, Pavel Urbánek, Michal Machovsky, David Skoda, Milan Masař, Martin Holek, Sonochemical synthesis of Gd^{3+} doped $CoFe_2O_4$ spinel ferrite nanoparticles and its physical properties, Ultra Sonochem. 40 (2018) 773–783.

[17] A.V. Mahulkar, C. Riedel, P.R. Gogate, U. Neis, A.B. Pandit, Effect of dissolved gas on efficacy of sonochemical reactors for microbial cell disruption: experimental and numerical analysis, Ultra Sonochem. 16 (2009) 635–643.

[18] D.V. Pinjari, A.B. Pandit, Cavitation milling of natural cellulose to nanofibrils, Ultra Sonochem. 17 (2010) 845–852.

[19] M. Ashokkumar, Ultrasonic Synthesis of Functional Materials, Springer Briefs in Green Chemistry for Sustainability, Springer, 2016.

[20] M. Maria Lumina Soniaa, S. Anand, V. Maria Vinosel, M. Asisi Janifer, S. Pauline, A. Manikandan, Effect of lattice strain on structure, morphology and magneto-dielectric properties of spinel $NiGd_xFe_{2-x}O_4$ ferrite nano-crystallites synthesized by sol-gel route, J. Magn. Magn. Mater. 466 (2018) 238–251.

[21] R.S. Yadav, I. Kuřitka, J. Vilcakova, J. Havlica, L. Kalina, P. Urbánek, M. Machovsky, D. Skoda, M. Masař, M. Holek, Sonochemical synthesis of Gd^{3+} DOPED $CoFe_2O_4$ spinel ferrite nanoparticles and its physical properties, Ultrason. Sonochem. 40 (2018) 773–783.

[22] Suneetha Thota, Subhash C. Kashyap, Shiv K. Sharma, V.R. Reddy, Micro Raman, Mossbauer and magnetic studies of manganese substituted zinc ferrite nanoparticles: role of Mn, J. Phys. Chem. Solids 91 (2016) 136–144.

[23] M.H. Abdellatifa, A.A. Azaba, M. Salerno, Effect of rare earth doping on the vibrational spectra of spinel Mn-Cr ferrite, Mater. Res. Bull. 97 (2018) 260–264.

[24] E. F. Bertaut, Structures des boroferrites, Acad. Sci. Paris 230, 213 (1950); Errata, 231, 88 (1951).

[25] Sagar E. Shirsath, M.L. Mane, Y. Yasukawa, X. Liu, A. Morisako, Self-ignited high temperature synthesis and enhanced super-exchange interactions of Ho^{3+}–Mn^{2+}–Fe^{3+}–O^{2-} ferromagnetic nanoparticles, Phys. Chem. Chem. Phys. 16 (2014) 2347–2357.

[26] S. Nag, A. Roychowdhury, D. Das, S. Das, S. Mukherjee, Structural and magnetic properties of erbium (Er^{3+}) doped nickel zinc ferrite prepared by sol-gel auto-combustion method, J. Magn. Magn. Mater. 466 (2018) 172–179.

[27] R. Kumar, M. Kar, Correlation between lattice strain and magnetic behavior in non-magnetic Ca substituted nano-crystalline cobalt ferrite, Ceram. Int. 42 (6) (2016) 6640–6647.

[28] S.I. Ahmad, S.A. Ansari, D.R. Kumar, Structural, morphological, magnetic properties and cation distribution of Ce and Sm co-substituted nano crystalline cobalt ferrite, Mater. Chem. Phys. 208 (2018) 248–257.

[29] B.D. Cullity, C.D. Graham, Introduction to Magnetic Materials, second ed., Wiley-IEEE Press, 2008 ISBN 978-0-471-47741-9.

[30] S.I. Ahmad, D.R. Kumar, I.A. Syed, R. Satar, S.A. Ansari, Structural, spectroscopic and magnetic study of nanocrystalline cerium-substituted magnesium ferrites, Arabian J. Sci. Eng. 42 (2017) 389–398.

[31] J. Tauc, R. Grigorovici, A. Vancu, Optical properties and electronic structure of amorphous germanium, Phys. Status solidi 15 (1966) 627–637.

[32] A. Baykal, S. Esir, A. Demir, S. Güner, Magnetic and optical properties of $Cu_{1-x}Zn_xFe_2O_4$ nanoparticles dispersed in a silica matrix by a sol-gel auto-combustion method, Ceram. Int. 41 (2015) 231–239.

[33] A. Baykal, S. Güner, A. Demir, S. Esir, F. Genç, Effects of Zinc substitution on magneto-optical properties of $Mn_{1-x}Zn_xFe_2O_4/SiO_2$ nanocomposites, Ceram. Int. 40 (2014) 13401–13408.

[34] E.A. Davis, N.F. Mott, Conduction in non-crystalline systems V Conductivity, optical absorption and photoconductivity in amorphous semiconductors, Philos. Magazine 179 (1970) 903–922.

[35] N.F. Mott, E.A. Davis, Electronic Processes in Non-crystalline Materials, second ed., Clarendon Press (Oxford and Newyork), 1979.

[36] S. Asiri, M. Sertkol, S. Güner, H. Güngüneş, K.M. Batoo, T.A. Saleh, H. Sözeri, M.A. Almessiere, A. Manikandan, A. Baykal, Hydrothermal synthesis of $Co_yZn_yMn_{1-2y}Fe_2O_4$ nanoferrites: magneto-optical investigation, Ceram. Int. 44 (5) (2018) 5751–5759.

[37] N.R. Yogamalar, A.C. Bose, Burstein-Moss shift and room temperature near-band-edge luminescence in lithium-doped zinc oxide, Appl. Phys. A 103 (2011) 33–42.

[38] R.S. Melo, P. Banerjee, A. Franco Jr, Hydrothermal synthesis of nickel doped ferrite nanoparticles: optical and magnetic properties, J. Mater. Sci.: Mater. Elect. 17 (2018) 14657–14667.

[39] T.E.P. Alves, H.V.S. Pessoni, A. Franco Jr, The effect of Y^{3+} subsitution on the structural, optical band-gap, and magnetic properties of Cobalt ferrite nanoparticles, Phys. Chem. Chem. Phys. 19 (2017) 16395.

[40] S. Supriya, S. Kumar, M. Kar, Band gap engineering of Z substituted cobalt ferrite for optoelectronic applications, IEEE, Nanotechnology Material and Devices Conference, (2017) Singapore.

[41] M. Saha, S. Mukherjee, A. Gayen, Microstructure, optical and magnetic properties of inverse spinel $CoFe_2O_4$ synthesized by microemulsion process assisted by CTAB and AOT, J. Aust. Ceram. Soc. 52 (2016) 150–162.

[42] J.L.O. Quinonez, U. Pal, M.S. Villanueva, Structural, magnetic, and catalytic evaluation of spinel Co, Ni, and Co-Ni ferrite nanoparticles fabricated by low-temperature solution combustion process, ACS Omega 3 (2018) 14986–15001.
[43] E.C. Stoner, E.P. Wohlfarth, A mechanism of magnetic hysteresis in heteregeneous alloys, Philos. Trans. Royal Soc. A 240 (826) (1948) 599–642.
[44] M.A. Almessiere, A. Demir Korkmaz, Y. Slimani, M. Nawaz, S. Ali, A. Baykal, Magneto-optical properties of rare earth metals substituted Co-Zn spinel nano-ferrites, Ceram. Int. 45 (2019) 3449–3458.
[45] M.A. Almessiere, Y. Slimani, H.S. El Sayed, A. Baykal, Ca^{2+} and Mg^{2+} incorporated barium hexaferrites: structural and magnetic properties, J. Sol-Gel Sci. Technol. 88 (2018) 628–638.
[46] Y. Slimani, H. Güngüneş, M. Nawaz, A. Manikandan, H.S. El Sayed, M.A. Almessiere, H. Sözeri, S.E. Shirsath, I. Ercan, A. Baykal, Magneto-optical and microstructural properties of spinel cubic copper ferrites with Li-Al co-substitution, Ceram. Int. 44 (2018) 14242–14250.
[47] M.A. Almessiere, Y. Slimani, A. Baykal, Structural and magnetic properties of Ce doped strontium hexaferrite, Ceram. Int. 44 (2018) 9000.
[48] F.X. Chen, J.T. Jia, Z.G. Xu, B. Zhou, C.S. Liao, C.H. Yan, L.Y. Chen, H.B. Zhao, Microstructure, magnetic, and magneto-optical properties of chemical synthesized Co-RE (RE = Ho, Er, Tm, Yb, Lu) ferrite nanocrystalline films, J. Appl. Phys. 86 (1999) 2727.
[49] M.A. Almessiere, Y. Slimani, S. Ali, A. Baykal, I. Ercan, H. Sozeri, Nd^{3+} ion substituted $Co_{1-2x}Ni_xMn_xFe_{2-y}O_4$ nanoparticles: structural, morphological and magnetic investigations, J. Inorg. Organomet. Polym. (2018), https://doi.org/10.1007/s10904-018-1052-z.
[50] Y. Slimani, M.A. Almessiere, M. Nawaz, A. Baykal, S. Akhtar, I. Ercan, I. Belenli, Effect of bimetallic (Ca, Mg) substitution on magneto-optical properties of $NiFe_2O_4$ nanoparticles, Ceram. Int. (2019), https://doi.org/10.1016/j.ceramint.2018.12.072.
[51] A.K. Nikumbh, R.A. Pawar, D.V. Nighot, G.S. Gugale, M.D. Sangale, M.B. Khanvilkar, A.V. Nagawade, Structural, electrical, magnetic and dielectric properties of rare-earth substituted cobalt ferrites nanoparticles synthesized by the co-precipitation method, J. Magn. Magn. Mater. 355 (2014) 201–209.
[52] M. Raghasudha, D. Ravinder, P. Veerasomaiah, Magnetic properties of Cr-substituted Co-ferrite nanoparticles synthesized by citrate-gel autocombustion method, J. Nanostruct. Chem. 3 (2013) 63.
[53] S. Singhal, S.K. Barthwal, K. Chandra, XRD, magnetic and Mössbauer spectral studies of nano size aluminum substituted cobalt ferrites ($CoAl_xFe_{2-x}O_4$), J. Magn. Magn. Mater. 306 (2006) 233–240.
[54] R. Nongjai, S. Khan, K. Asokan, H. Ahmed, I. Khan, Magnetic and electrical properties of In doped cobalt ferrite nanoparticles, J. Appl. Phys. 112 (2012) 084321.
[55] M.A. Almessiere, Y. Slimani, A. Baykal, Impact of Nd-Zn co-substitution on microstructure and magnetic properties of $SrFe_{12}O_{19}$ nanohexaferrite, Ceram. Int. 45 (2019) 963–969.
[56] M.A. Almessiere, Y. Slimani, H.S. EL Sayed, A. Baykal, Morphology and magnetic traits of strontium nanohexaferrites: effects of manganese/yttrium co-substitution, J. Rare Earths (2019), https://doi.org/10.1016/j.jre.2018.09.014.
[57] M.A. Almessiere, Y. Slimani, N.A. Tashkandi, A. Baykal, M.F. Saraç, A.V. Trukhanov, İ. Ercan, İ. Belenli, B. Ozçelik, The effect of Nb substitution on magnetic properties of $BaFe_{12}O_{19}$ nanohexaferrites, Ceram. Int. 45 (2019) 1691–1697.
[58] M.A. Almessiere, Y. Slimani, H.S. El Sayed, A. Baykal, I. Ercan, Microstructural and magnetic investigation of vanadium-substituted Sr-nanohexaferrite, J. Magn. Magn. Mater. 471 (2019) 124–132.
[59] M.A. Almessiere, Y. Slimani, H.S. El Sayed, A. Baykal, S. Ali, I. Ercan, Investigation of microstructural and magnetic properties of $BaV_xFe_{12-x}O_{19}$ nanohexaferrites, J. Supercond. Novel Magn. (2018), https://doi.org/10.1007/s10948-018-4856-8.
[60] M.A. Almessiere, Y. Slimani, A. Baykal, Structural morphological and magnetic properties of hard/soft $SrFe_{12-x}V_xO_{19}/(Ni_{0.5}Mn_{0.5}Fe_2O_4)_y$ nanocomposites: effect of vanadium substitution, J. Alloys Compd. 767 (2018) 966–975.
[61] M.A. Almessiere, Y. Slimani, A. Baykal, Exchange spring magnetic behavior of $Sr_{0.3}Ba_{0.4}Pb_{0.3}Fe_{12}O_{19}/(CuFe_2O_4)_x$ nanocomposites fabricated by a one-pot citrate sol-gel combustion method, J. Alloys Compd. 762 (2018) 389–397.
[62] Md Amir, H. Gungunes, Y. Slimani, N. Tashkandi, H.S. El Sayed, F. Aldakheel, M. Sertkol, H. Sozeri, A. Manikandan, I. Ercan, A. Baykal, Mossbauer studies and magnetic properties of cubic $CuFe_2O_4$ nanoparticles, J. Supercond. Novel Magn. (2018), https://doi.org/10.1007/s10948-018-4733-5.
[63] Y. Slimani, A. Baykal, Md. Amir, N. Tashkandi, H. Güngüneş, S. Guner, H.S. El Sayed, F. Aldakheel, T.A. Saleh, A. Manikandan, Substitution effect of Cr^{3+} on hyperfine interactions, magnetic and optical properties of Sr-hexaferrites, Ceram. Int. 44 (2018) 15995–16004.
[64] M.A. Almessiere, Y. Slimani, H.S. El Sayed, A. Baykal, Structural and magnetic properties of Ce-Y substituted Strontium nanohexaferrites, Ceram. Int. 44 (2018) 12511–12519.
[65] A.D. Korkmaz, S. Güner, Y. Slimani, H. Gungunes, Md. Amir, A. Manikandan, A. Baykal, Microstructural, optical and magnetic properties of vanadium substituted nickel spinel nano-ferrites, J. Supercond. Nov. Magn. (2018), https://doi.org/10.1007/s10948-018-4793-6.
[66] I. Ali, M.U. Islam, M.S. Awan, M. Ahmad, M.N. Ashiq, S. Naseem, Effect of Tb^{3+} substitution on the structural and magnetic properties of M-type hexaferrites synthesized by sol–gel auto-combustion technique, J. Alloys Compd. 550 (2013) 564–572.